JOURNAL OF APPLIED PHYSICS **117**, 064505 (2015)

Contact behavior evolution induced by damage growth in radio-frequency microelectromechanical system switches

Y. Wu[a] and D. Peroulis
Birck Nanotechnology Center, School of Electrical and Computer Engineering, Purdue University, West Lafayette, Indiana 47907-2035, USA

(Received 8 November 2014; accepted 28 January 2015; published online 10 February 2015)

This study provides a two-contact-event model to explain the evolution of the contact behavior of microelectromechanical system (MEMS) switches through their lifetime. The succession of two dynamic contact events is carefully considered during actuation inspired by experimental observations. The contact between the MEMS switch tip and the drain can be treated as an effective contact between an elastic hemisphere and a rigid plane. If the first contact event results in elastic deformation, the effective hemisphere will fully recover. Consequently, the subsequent contact event also produces elastic deformation. If, on the other hand, the first contact event induces elastoplastic or plastic deformation, a residual depth will be produced between the hemisphere and the rigid plane. The contact force of the subsequent contact event can be significantly reduced due to this additional residual depth. With the growth of residual depth during the switch cycling process, the modeling results show three possible situations of contact radius evolution: (1) The contact radius increases to a maximum value and then decreases to zero; (2) the contact radius increases to one local maximum value; then decreases to a local minimum value; subsequently increases again to another maximum value, and finally decreases to zero; and (3) the contact radius increases to one maximum value and then decreases to zero; after an intermittent response, the contact radius increases again to another maximum value and finally decreases to zero. Furthermore, the Maxwell spreading formula is applied to determine the contact resistance which is inversely proportional to the contact radius. Three situations of contact resistance evolution corresponding to the evolution of contact radius are obtained. All three situations are also observed and validated by the experimental results. © *2015 AIP Publishing LLC*.
[http://dx.doi.org/10.1063/1.4907803]

I. INTRODUCTION

Contact damage is a significant factor limiting the lifetime of a radio-frequency microelectromechanical system (RF MEMS) switch. Majumder *et al.*[1,2] developed a simplified adhesive contact model for the elastoplastic and fully plastic contact between the contact tip and the drain of a MEMS switch to investigate the contact resistance versus the contact force in a single contact event. McGruer *et al.*[3] used a scanning-probe-microscope-(SPM)-based contact test station to emulate the contact of a MEMS switch. They presented variations of contact resistance between different alloys versus switching cycles and scanning electron microscope (SEM) images of a damaged contact bump at different switching cycles. Hennessy *et al.*[4] investigated the damage of ruthenium-on-ruthenium contacts by using an SPM-based contact test system. They compared the lifetime of contacts for three cases: (1) no voltage applied at the contact interface during contact, (2) voltage applied at the contact interface only during contact (cold switching), and (3) voltage always applied between the contact tip and the drain during contact and separation (hot switching). They showed that hot switching causes the worst contact damage under the same switching cycles. It has also been demonstrated that the current which flows through the contact region causes the local temperature then to rise and then soften the contact materials.[5–7] The softening effect can induce worse damage under the same contact force.

Contact damage between two non-conformal bodies has been investigated by both analytical and finite element methods. Chang *et al.*[8] (CEB model) developed an analytical model of the elastic and fully plastic deformation for an asperity on a rough surface. However, the transition between these two states, called "elastoplastic deformation," is excluded in their model. Zhao *et al.*[9] (ZMC model) used a mathematical method to obtain a smooth transition of the contact radius, mean contact pressure, and contact force between the elastic and fully plastic deformation of a single asperity. It is noted that adhesion is neglected at the contact interface in both the CEB and ZMC models. Kogut and Etsion[10] compared the finite element simulations to the CEB and ZMC models. The results show that the ZMC model is closer to the finite element simulation than the CEB model. It is noted that the unknown analytical shape and size of the elastic-plastic boundary significantly complicate the inclusion of adhesion into any analytical contact model. Hence, the finite element method is often used to investigate contact phenomena including the adhesion from elastic to fully plastic deformation.[11–13] The finite element simulations also reveal that the deformation in a large loading process is

[a]Electronic mail: wu639@purdue.edu

almost independent of the material properties even with adhesion.[11,12]

When the actuation voltage is applied between the switch beam and the gate, the electrostatic force bends the beam toward the gate and makes the beam tip contact the drain surface. The steeply rising actuation voltage induces a high kinetic energy on the switch beam. Hence, the beam tip cannot be captured by the drain surface at the first time of the tip-drain contact during actuation. Consequently, the beam tip may leave and then contact the drain again for several times until the kinetic energy is almost eliminated. These contact events produce several dynamic bounces during actuation.[14–16] It should be noted that the maximum contact force at the first contact event is larger than the maximum contact forces at subsequent contact events due to the highest kinetic energy at the first contact event.

This study presents the analytical study to illustrate the evolution of contact behavior. During each contact event, only the final maximum deformation needs to be considered. It is noted that this maximum deformation is produced during the loading process of each contact event. In addition, the loading of contact is independent of adhesion. Thus, the ZMC model can be used to predict the contact between the switch beam tip and the drain from the elastic deformation to the plastic deformation. When the first contact event is elastic, the subsequent contact events will produce elastic deformation. When the first contact event causes the elastoplastic or fully plastic deformation, the contact damage can reduce the contact forces in the subsequent contact events. With the growth of contact damage, the evolution of contact behavior can be obtained. In addition, non-dimensionalized parameters are used into the analysis. Hence, no necessary information is needed on the dimensions and material properties of a MEMS switch. Such non-dimensionalized analysis can be applied for various contact materials with substituting the material properties into the dimensionless results.

II. CONTACT DAMAGE MODELING

The switches tested in this study are packaged, and there is not sufficient information on the exact geometry of the contact tip. However, Rezvanian *et al.*[17] discovered that very few asperities of the gold bump of a MEMS switch make contact and conduct the electrical current. Hence, in this study, the contact tip and drain of the switch are assumed to be sufficiently smooth to neglect multi-scale contact effects. The contact between the contact tip and the drain can be simply considered as the equivalent contact between an elastic hemisphere with an effective radius of curvature R and a rigid flat plane as shown in Fig. 1. The effective elastic modulus E^* of the elastic hemisphere is defined as

$$\frac{1}{E^*} = \frac{1-\nu_t^2}{E_t} + \frac{1-\nu_d^2}{E_d}, \tag{1}$$

where E_t and ν_t are the Young's modulus and Poisson's ratio of the switch tip, and E_d and ν_d are the Young's modulus and Poisson's ratio of the drain. In each contact event, the contact force F produces a pair of the maximum radius of the contact area a and the interference δ. The interference δ is defined as the distance between the summit of the undeformed hemisphere and the summit of the fully loaded hemisphere. It must be noted that a positive contact force F leads to a positive interference δ when the sphere is in compression.

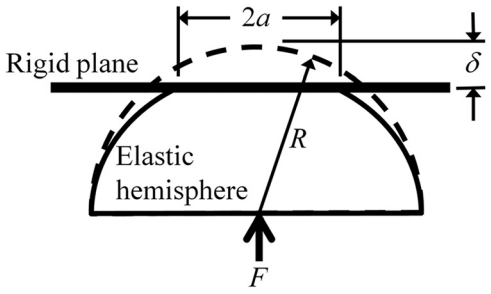

FIG. 1. The equivalent contact model of an elastic hemisphere with radius of curvature R and a rigid flat plane: the broken hemisphere for the undeformed shape, and the solid hemisphere for the fully loaded shape.

A. Elastic contact (Hertz model)

During loading, the maximum radius of contact area a_i, the maximum mean contact pressure p_{mi}, and the maximum contact force F_i dependent on the maximum interference δ_i are given by

$$a_i = \sqrt{R\delta_i}, \tag{2}$$

$$p_{mi} = \frac{4E^* a_i}{3\pi R}, \tag{3}$$

$$F_i = \frac{4}{3}E^* R^{1/2}\delta_i^{3/2}, \tag{4}$$

where the subscript i presents the maximum value of the parameter during the ith contact event per switching cycle.

The critical interference δ_c for the onset of yield is given by[8]

$$\delta_c = \left(\frac{\pi KH}{2E^*}\right)^2 R, \tag{5}$$

where H is the hardness of the elastic hemisphere which is related to the yield strength Y, i.e., $H \approx 2.8Y$, and K is the hardness coefficient

$$K = 0.454 + 0.41\nu, \tag{6}$$

where ν is the effective Poisson's ratio. By substituting Eqs. (2) and (5) into Eq. (3), the critical mean contact pressure for the onset of yield is obtained as

$$p_{mc} = \frac{2}{3}KH \approx 1.87KY. \tag{7}$$

Therefore, the deformation of the hemisphere is elastic when the mean contact pressure p_m is lower than p_{mc}.

B. Elastoplastic contact

When the mean contact pressure p_m exceeds p_{mc}, the elastoplastic deformation occurs. The relationship among a_i, p_{mi}, and F_i are given by[9]

$$a_i^2 = R\delta_i\left[1 - 2\left(\frac{\delta_i - \delta_c}{\delta_p - \delta_c}\right)^3 + 3\left(\frac{\delta_i - \delta_c}{\delta_p - \delta_c}\right)^2\right], \quad (8)$$

$$p_{mi} = H - H\left(1 - \frac{2}{3}K\right)\frac{\ln\delta_p - \ln\delta_i}{\ln\delta_p - \ln\delta_c}, \quad (9)$$

$$F_i = \pi R\delta_i H\left[1 - \left(1 - \frac{2}{3}K\right)\frac{\ln\delta_p - \ln\delta_i}{\ln\delta_p - \ln\delta_c}\right] \times \left[1 - 2\left(\frac{\delta_i - \delta_c}{\delta_p - \delta_c}\right)^3 + 3\left(\frac{\delta_i - \delta_c}{\delta_p - \delta_c}\right)^2\right], \quad (10)$$

where δ_p is the critical interference of the onset of fully plastic deformation which is discussed in Sec. II C.

C. Fully plastic contact

When the mean contact pressure p_m reaches the value of the hardness H ($H \approx 2.8Y$), the contact region of the hemisphere becomes fully plastic. The relationship among a_i, p_{mi}, and F_i are given by[18]

$$a_i = \sqrt{2R\delta_i}, \quad (11)$$

$$p_{mi} = H, \quad (12)$$

$$F_i = 2\pi HR\delta_i. \quad (13)$$

A ratio of the critical contact area of the onset of fully plastic deformation A_p to the critical contact area of the onset of yield A_c has to be introduced as[19]

$$c_A = \frac{A_p}{A_c}. \quad (14)$$

The value of c_A is estimated by experimental results. It is noted that $A_p = \pi a_p{}^2 = 2\pi R\delta_p$ from Eq. (11) and $A_c = \pi a_c{}^2 = \pi R\delta_c$ from Eq. (2). Thus, the relationship between δ_p and δ_c can be found as

$$\delta_p = \frac{c_A}{2}\delta_c. \quad (15)$$

D. Unloading process

If the loading results in elastic deformation, i.e., $p_{mi} < p_{mc}$, the hemisphere can fully recover to the original undeformed shape. If the loading leads to elastoplastic or plastic deformation, i.e., $p_{mi} > p_{mc}$, a permanent deformation will occur. Contact damage can be obtained after unloading. Johnson[18] assumed that the unloading process is elastic. The comparison results show that the modeled elastic recovery matches the experimental data very well. According to Johnson's assumption, the effective radius of curvature R_{eff} after unloading is given by

$$R_{eff} = \frac{4a_iE^*}{3\pi p_{mi}}, \quad (16)$$

where a_i and p_{mi} are the maximum radius of the contact area and the maximum mean contact pressure caused by the maximum contact force F_i during the prior loading, respectively.

After unloading, the permanent deformation results in a residual depth δ_{res} between the summits of the undamaged hemisphere and the damaged hemisphere

$$\delta_{res} = \delta_i - \frac{a_i^2}{R_{eff}}, \quad (17)$$

where δ_i is the maximum interference caused by the maximum contact force F_i during the prior loading.

E. Subsequent loadings

If the prior loading causes elastic contact, no contact damage will be produced after unloading. The radius of curvature of the hemisphere does not change. Hence, the equations from Secs. II A to II C are still valid for the next loading. If the elastoplastic or plastic deformation is produced during the prior loading, the permanent deformation will change the radius of curvature R_{eff} of the hemisphere as in Eq. (16) and leave a residual depth δ_{res} as in Eq. (17) after unloading. Due to the change of the radius of curvature, all R values in Eqs. (2)–(13) need to be replaced with R_{eff} to determine the maximum contact radius a_i, the maximum mean contact pressure p_{mi}, and the maximum contact force F_i. It should also be noted that the hemisphere deforms from the elastic state in each subsequent loading since the unloading process is elastic. Furthermore, the critical values of the mean contact pressure at the onset of yield, p_{mc} (Eq. (7)), and fully plastic deformation, $p_m = H$, are independent of the radius of curvature of the hemisphere. Thus, the change of the radius of curvature does not affect p_{mc} and H.

F. Non-dimensionalization

For non-dimensionalization, the dimensionless parameters below should be introduced

$$\text{Dimensionless contact radius}: a^* = \frac{4E^*a}{3\pi RY}, \quad (18a)$$

$$\text{Dimensionless interference}: \delta^* = \left(\frac{4E^*}{3\pi Y}\right)^2\frac{\delta}{R}, \quad (18b)$$

$$\text{Dimensionless mean contact pressure}: p_m^* = \frac{p_m}{Y}, \quad (18c)$$

$$\text{Dimensionless contact force}: F^* = \frac{16E^{*2}F}{9\pi^3R^2Y^3}. \quad (18d)$$

In the following analysis, because the critical values of the mean contact pressure of the onset of yield and fully plastic deformation are independent of the radius of curvature of the hemisphere, the dimensionless critical interference $\delta_c{}^*$ for the onset of yield is replaced by the dimensionless critical mean contact pressure $p_{mc}{}^*$ through using the relationship between Eqs. (18b) and (18c), i.e., $\delta_c{}^* = p_{mc}{}^{*2}$. Then the dimensionless critical interference $\delta_p{}^*$ of the onset of fully plastic deformation can be written as: $\delta_p{}^* = c_A\delta_c{}^*/2 = c_A p_{mc}{}^{*2}/2$. It should be noted that $p_{mc}{}^* = 1.87$ K.

By substituting these dimensionless parameters above, Eqs. (2)–(13) for a contact event without damage prior to the loading process can be written as

(a) *Elastic contact* ($p^*_{mi} \le 1.87\text{K}$):

$$a_i^* = \sqrt{\delta_i^*}, \tag{19}$$

$$p_{mi}^* = \sqrt{\delta_i^*}, \tag{20}$$

$$F_i^* = \delta_i^{*3/2}. \tag{21}$$

(b) *Elastoplastic contact* ($1.87\text{K} \le p^*_{mi} \le 2.8$):

$$a_i^{*2} = \delta_i^* \left\{ 1 - 2\left[\frac{\delta_i^* - p_{mc}^{*2}}{\left(\frac{C_A}{2}-1\right)p_{mc}^{*2}}\right]^3 + 3\left[\frac{\delta_i^* - p_{mc}^{*2}}{\left(\frac{C_A}{2}-1\right)p_{mc}^{*2}}\right]^2 \right\}, \tag{22}$$

$$p_{mi}^* = 2.8 - 2.8\left(1 - \frac{2}{3}K\right)\left[\frac{\ln\left(\frac{C_A}{2}p_{mc}^{*2}\right) - \ln\delta_i^*}{\ln\left(\frac{C_A}{2}p_{mc}^{*2}\right) - 2\ln p_{mc}^*}\right], \tag{23}$$

$$F_i^* = 2.8\delta_i^* \left\{ 1 - \left(1 - \frac{2}{3}K\right)\left[\frac{\ln\left(\frac{C_A}{2}p_{mc}^{*2}\right) - \ln\delta_i^*}{\ln\left(\frac{C_A}{2}p_{mc}^{*2}\right) - 2\ln p_{mc}^*}\right] \right\} \times \left\{ 1 - 2\left[\frac{\delta_i^* - p_{mc}^{*2}}{\left(\frac{C_A}{2}-1\right)p_{mc}^{*2}}\right]^3 + 3\left[\frac{\delta_i^* - p_{mc}^{*2}}{\left(\frac{C_A}{2}-1\right)p_{mc}^{*2}}\right]^2 \right\}. \tag{24}$$

(c) Fully plastic contact ($p_{mi}{}^* = 2.8$)

$$a_i^* = \sqrt{2\delta_i^*}, \tag{25}$$

$$p_{mi}^* = 2.8, \tag{26}$$

$$F_i^* = 5.6\delta_i^*. \tag{27}$$

If the loading leads to elastoplastic or fully plastic deformation, the radius of curvature of the hemisphere will change to R_{eff} after unloading. Hence, the dimensionless effective radius of curvature of the hemisphere is defined as

$$R_{eff}^* = \frac{R_{eff}}{R} = \frac{a_i^*}{p_{mi}^*}. \tag{28}$$

The dimensionless residual depth can be written as

$$\delta_{res}^* = \delta_i^* - p_{mi}^* a_i^*. \tag{29}$$

If the radius of curvature does not change after unloading, Eqs. (19)–(27) will still be valid for the next contact event. If the radius of curvature changes after unloading, the contact parameters in the next contact event will be determined by

(d) *Elastic contact* ($p^*_{mi} \le 1.87\text{K}$):

$$a_i^* = \sqrt{R_{eff}^* \delta_i^*}, \tag{30}$$

$$p_{mi}^* = \sqrt{\frac{\delta_i^*}{R_{eff}^*}}, \tag{31}$$

$$F_i^* = \sqrt{R_{eff}^*}\,\delta_i^{*3/2}. \tag{32}$$

(e) *Elastoplastic contact* ($1.87\text{K} \le p^*_{mi} \le 2.8$):

$$a_i^{*2} = R_{eff}^* \delta_i^* \left\{ 1 - 2\left[\frac{\delta_i^*/R_{eff}^* - p_{mc}^{*2}}{\left(\frac{C_A}{2}-1\right)p_{mc}^{*2}}\right]^3 + 3\left[\frac{\delta_i^*/R_{eff}^* - p_{mc}^{*2}}{\left(\frac{C_A}{2}-1\right)p_{mc}^{*2}}\right]^2 \right\}, \tag{33}$$

$$p_{mi}^* = 2.8 - 2.8\left(1 - \frac{2}{3}K\right)\left[\frac{\ln\left(\frac{C_A}{2}p_{mc}^{*2}\right) - \ln\left(\delta_i^*/R_{eff}^*\right)}{\ln\left(\frac{C_A}{2}p_{mc}^{*2}\right) - 2\ln p_{mc}^*}\right], \tag{34}$$

$$F_i^* = 2.8\delta_i^* \left\{ 1 - \left(1 - \frac{2}{3}K\right)\left[\frac{\ln\left(\frac{C_A}{2}p_{mc}^{*2}\right) - \ln\delta_i^*}{\ln\left(\frac{C_A}{2}p_{mc}^{*2}\right) - 2\ln p_{mc}^*}\right] \right\} \times \left\{ 1 - 2\left[\frac{\frac{\delta_i^*}{R_{eff}^*} - p_{mc}^{*2}}{\left(\frac{C_A}{2}-1\right)p_{mc}^{*2}}\right]^3 + 3\left[\frac{\frac{\delta_i^*}{R_{eff}^*} - p_{mc}^{*2}}{\left(\frac{C_A}{2}-1\right)p_{mc}^{*2}}\right]^2 \right\}. \tag{35}$$

(f) Fully plastic contact ($p_{mi}{}^* = 2.8$)

$$a_i^* = \sqrt{2R_{eff}^*\delta_i^*}, \tag{36}$$

$$p_{mi}^* = 2.8, \tag{37}$$

$$F_i^* = 5.6R_{eff}^*\delta_i^*. \tag{38}$$

G. Relationship of contact forces among contact events

A typical electrostatic MEMS switch comprised of a cantilever or a doubly clamped beam can be effectively modeled by an elastic hemispherical tip connecting a spring with spring constant k_b and a rigid drain plane as shown in Fig. 2(a). In each contact event, an effective force F_E makes the beam tip contact the drain as shown in Fig. 2(b). It is noted that the kinetic energy is produced in the initial stage when an actuation voltage V is just applied. The largest kinetic energy accompanies the applied electrostatic force and results in the largest effective force F_{E1} in the first contact event. After each contact event, some of the kinetic energy is dissipated resulting in lower contact force for the subsequent contact events. A switch is settled when the kinetic energy is practically eliminated. When the switch is settled, the effective contact force F_{ES} depends on the applied voltage only and not on time.

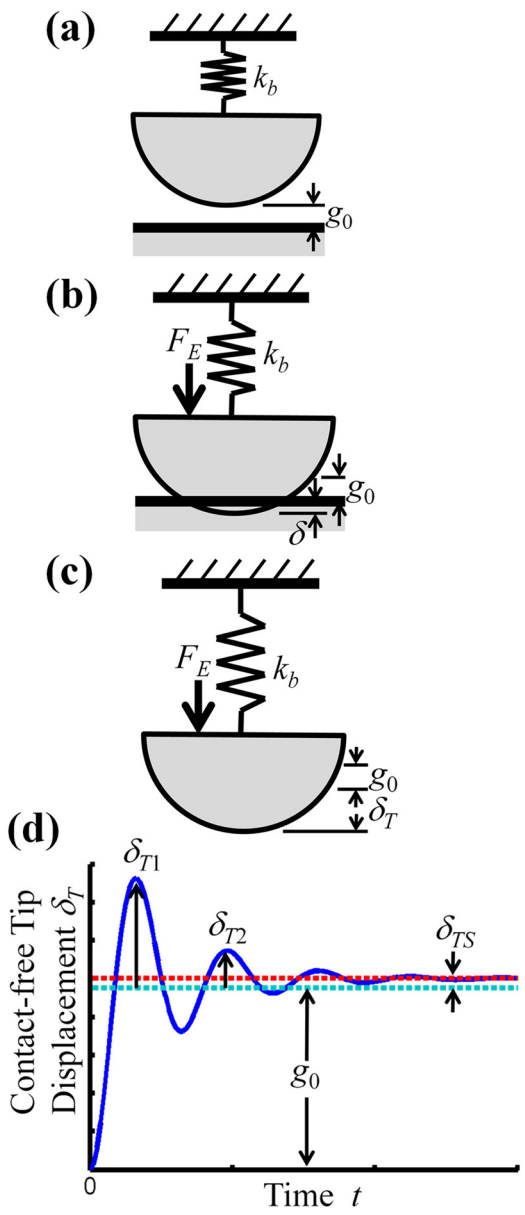

FIG. 2. Effective switch model: (a) the pre-actuated state, (b) the actuated state, (c) the actuated state without contact, and (d) the contact-free tip displacement vs. time.

If no drain surface was to be contacted by the tip as shown in Fig. 2(c), the effective force F_E would be able to cause a tip displacement equal to the summation of the tip-drain gap g_0 and the contact-free displacement δ_T, i.e., $F_E = k_b(g_0 + \delta_T)$. It must be noted that the contact-free displacement δ_T only depends on the magnitude and the rising rate of the given actuation voltage V. Figure 2(d) illustrates a typical contact-free displacement evolution during one switching cycle when a step-function-like actuation voltage is applied. The first maximum contact-free displacement δ_{T1} is always the greatest one due to the largest kinetic energy in the first contact event. Furthermore, the maximum contact force F_i in the i^{th} contact event is equal to $k_b\delta_{Ti}$ if no damage exists prior to loading. If the loading prior to the i^{th} contact event results in a residual depth δ_{res} on the summit of tip, the maximum contact force in the i^{th} contact event needs to be modified as: $F_i = k_b(\delta_{Ti} - \delta_{res})$. With applying the dimensionless parameters in Eq. (18), the maximum dimensionless contact force F^* in the i^{th} contact event can be written as

$$F_i^* = k_b^*(\delta_{Ti}^* - \delta_{res}^*), \tag{39}$$

where k_b^* is the dimensionless spring constant and defined as: $k_b^* = k_b/\pi RY$. Thus, the contact force becomes zero when the dimensionless residual depth δ_{res}^* is not smaller than the dimensionless contact-free displacement δ_T^*.

It is noted that the dimensionless spring constant k_b^*, the dimensionless interference δ^*, and dimensionless contact force F^* are inversely proportional to the yield strength Y, the square of the yield strength Y^2, and the cube of the yield strength Y^3, respectively. Hence, for the convenience of calculation, the value of the dimensionless spring constant is estimated by

$$k_b^* = B\sqrt{\delta_{TS}^*}, \tag{40}$$

where B is an experimentally determined proportionality constant.

As shown in Fig. 2(d), the kinetic energy of the switch beam leads to several contact-free tip displacements δ_{Ti}^* greater than the settled contact-free tip displacement δ_{TS}^* in every switching cycle. Hence, the contact-free tip amplitudes δ_{Ti}^* in the i^{th} contact event can be represented proportionally to the settled contact-free tip displacement δ_{TS}^* as

$$\delta_{Ti}^* = n_i\delta_{TS}^* \quad (n_i > 1), \tag{41}$$

where n_i is a proportionality constant of the i^{th} contact-free tip displacement.

Summarizing, with a determined δ_{T1}^* by Eq. (41) with a given δ_{TS}^*, the maximum dimensionless contact force F_1^* can be determined by Eq. (39) in the first contact event per switching cycle. It must also be noted that the contact-free displacement δ_{T1}^* in the first contact event depends on the rising rate of the actuation voltage, and so does F_1^*. In this study, a steeply rising actuation voltage is given to operate the switch. Hence, the maximum contact force in the first contact event is always the greatest compared to all the maximum contact forces in the subsequent contact events. With a determined F_1^*, the maximum contact radius a_1^*, the maximum interference δ_1^*, and the maximum mean contact pressure p_{m1}^* can be obtained by Eqs. (19)–(21) for the elastic contact, Eqs. (22)–(24) for the elastoplastic contact, and Eqs. (25)–(27) for the plastic contact.

The subsequent maximum contact force F_i^* can be determined by Eq. (39) with a given δ_{Ti}^* and δ_{res}^*. If F_1^* causes an elastic deformation in the first contact event, Eqs. (19)–(27) will be still valid for the subsequent contact event with a determined F_i^*. If an elastoplastic or plastic deformation is produced by F_1^*, the effective radius of curvature of the hemisphere after unloading has to be determined by Eq. (28), and the residual depth δ_{res}^* at the summit of the hemisphere can be obtained by Eq. (29). Consequently, with a determined F_i^* and given R_{eff}^*, the maximum contact radius a_i^*, the maximum interference δ_i^*, and the maximum mean

contact pressure p_{mi}* can be obtained by Eqs. (30)–(32) for the elastic contact, Eqs. (33)–(35) for the elastoplastic contact, and Eqs. (36)–(38) for the plastic contact.

III. EXPERIMENTAL METHOD

The Omron 2SMES-01 switch was chosen as a device under test in this study due to its single-crystal-silicon structure, and hermetic packaging. The switch was tested beyond its manufacturer's specifications under hot switching condition. Specifically, the switching voltage was maintained between 8 and 10 V which is 20 times higher than the manufacturer's specified switching voltage (0.5 V). The switches were tested at multiplied applied voltages of 29, 34, and 39 V throughout their lifetimes. The operation and test conditions for these switches are summarized in Table I.

The experimental setup employs Fruehling's *et al.*[20] test procedure. The applied voltage supplied by an Agilent H5741A power supply was designed to produce a steep rise time. The switching voltage was provided by an Agilent N6705B power analyzer. Every 1×10^6 switching cycles operated at the same applied voltage of 29, 34, or 39 V, a sweep of applied voltages from 29 V to 39 V was conducted with 1 V increments to record the electrical features, i.e., switching voltage and contact resistance, at each recorded applied voltage.

IV. DISCUSSION

A. Modeling results

Hot switching has been demonstrated to induce the temperature around the contact region to rise due to Joule heating[4,5] and cold field electron emission[21] to soften contact materials. According to the modeling results of Ref. 21, such a high switching voltage (5 V) can increase the temperature on the surface of the contact materials, i.e., Au, Ru, and Pt, up to their melting points due to the cold field electron emission. This is consistent with our assumption that the contact tip is progressively getting softer versus switching cycles. Therefore, in the following analysis, this softening effect is reasonably assumed to cause δ_1* to increase as the switch is being cycled. This assumption indicates that the effective elastic modulus E*, yield strength Y, and interference δ_1 depend on the number of switching cycles. An increase in δ_1* also increases the corresponding dimensionless maximum contact radius a_1*, dimensionless maximum mean contact pressure p_{m1}*, and dimensionless maximum contact force F_1*.

TABLE I. Summary of testing conditions.

Parameter	Switch specifications	Test conditions
Applied voltage (V)	34±5%	29, 34, 39
Maximum applied voltage (V)	40	39
Minimum applied voltage (V)	N/A	24
Switching time (μs)	100	111
Switching voltage (V)	0.5	8–10
Switching current (mA)	0.5	1.8, 0.8

According to the experimental results, two cases were obtained: one with two observed contact events, and another with one observed contact event within one switching cycle. However, for the case of one observed contact event, the kinetic energy of the switch beam still causes a larger contact-free tip displacement in the initial stage than δ_{TS} of switching cycle as the purple line shown in Fig. 3. Hence, the case with one observed contact event can be considered as with two contact events because the initial larger contact-free tip displacement can result in worse damage than the settled contact-free tip displacement.

In the following calculation, the Poisson's ratio ν is taken to be 0.42 as the value of gold. This value results in the dimensionless critical mean contact pressure for the onset of yield p_{mc}* = 1.17. As the work of Johnson[18] that the contact force to cause the fully plastic deformation is at least 400 times that of the onset of yield, Zhao *et al.*[9] calculated that δ_p is at least 54 times δ_c, i.e., $\delta_p \geq 54\delta_c$. This value produces a fair value of $c_A = 108$ compared to several materials, e.g., $c_A \approx 60$ for phosphor-bronze, $c_A \approx 100$ for brass, and $c_A \approx 150$ for steel.[19] Therefore in this study, the proportionality constant c_A is taken to be 108, i.e., $\delta_p = 54\delta_c$. In addition, the proportionality constant B in Eq. (40) is assumed to be unity.

Figure 4 shows the evolution of dimensionless contact radii versus the increase in the dimensionless interference ratio δ_1*/δ_c* for different combinations of dimensionless contact-free displacements δ_{T1}* and δ_{TS}*. With δ_{T1}* increasing, three situations of contact radius evolution at the switch settled state can be obtained:

(a) *Situation 1* (δ_{T1}* $< 1.38\delta_{TS}$* or δ_{T1}* $> 1.48\delta_{TS}$*): The contact radius at the switch settled state increases up to a local maximum value and then decreases to zero (the green line and the purple line);
(b) *Situation 2* ($1.38\delta_{TS}^* \leq \delta_{T1}^* \leq 1.45\delta_{TS}^*$): The contact radius at the switch settled state increases to a local maximum, decreases to a local minimum, then increases to another local maximum, and finally decreases to zero (the light blue line);
(c) *Situation 3* ($1.45\delta_{TS}^* < \delta_{T1}^* \leq 1.48\delta_{TS}^*$): The contact radius at the switch settled state increases to a local

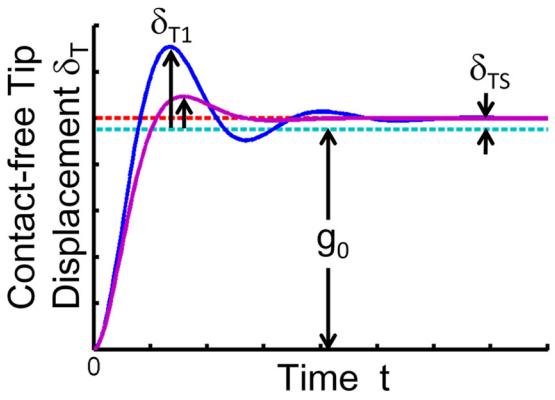

FIG. 3. Contact-free tip displacements vs. time for the cases with two observed contact events (blue line) and with one observed contact event (purple line) during one switching cycle.

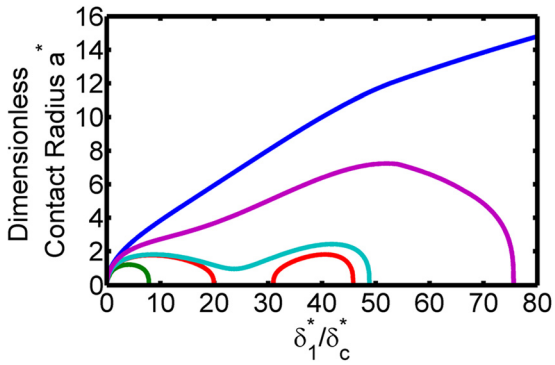

FIG. 4. Dimensionless contact radius a^* vs. δ_1^*/δ_c^*: the blue line is for the first contact event; the green line is for the settled contact with $\delta_{T1}^* = 2\delta_{TS}^*$; the red line is for the settled contact with $\delta_{T1}^* = 1.47\delta_{TS}^*$; the light blue line is for the settled contact with $\delta_{T1}^* = 1.45\delta_{TS}^*$, and the purple line is for the settled contact with $\delta_{T1}^* = 1.1\delta_{TS}^*$.

maximum and then decreases to zero; after an intermittent period, the contact radius increases again to another local maximum and finally decreases to zero (the red line).

Figure 5 presents the dimensionless mean contact pressure p_m^* versus δ_1^*/δ_c^* for the cases in Fig. 4. It is noted that the brown dotted line represents the dimensionless mean contact pressure p_{mc}^* for the onset of yield. Hence, the plastic deformation occurs when p_m^* is in the area above the brown dotted line. The tip remains elastic when p_m^* is in the area below the brown dotted line. In Fig. 5, p_{ms}^* at the switch settled state of the case with $\delta_{T1}^* = 2\delta_{TS}^*$ (green line) is always lower than the value of p_{mc}^*. For the cases with $\delta_{T1}^* = 1.45\delta_{TS}^*$ (light blue line) and $\delta_{T1}^* = 1.47\delta_{TS}^*$ (red line), p_{ms}^* increases to the value p_{mc}^* and then remains lower than p_{mc}^*. For the case with $\delta_{T1}^* = 1.1\delta_{TS}^*$ (purple line), p_{ms}^* can be higher than p_{mc}^* even until δ_1^* is around 60 times δ_c^*. It indicates that contact damage is also caused in the settled contact event.

Figure 6 illustrates the dimensionless contact force F^* versus δ_1^*/δ_c^* for the cases in Fig. 4. It is obvious that F_1^* is much greater than the values of F_S^*. It is noted that a

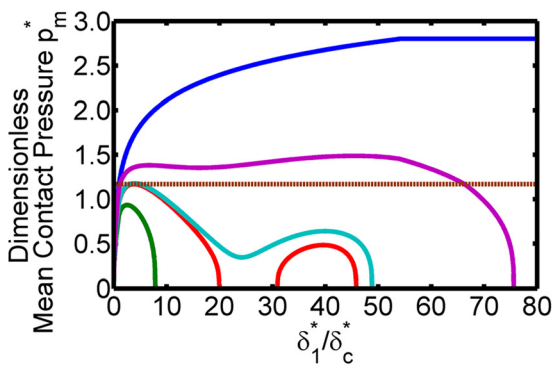

FIG. 5. Dimensionless mean contact pressure p_m^* vs. δ_1^*/δ_c^*: the blue line is for the first contact event; the green line is for the settled contact with $\delta_{T1}^* = 2\delta_{TS}^*$; the red line is for the settled contact with $\delta_{T1}^* = 1.47\delta_{TS}^*$; the light blue line is for the settled contact with $\delta_{T1}^* = 1.45\delta_{TS}^*$, and the purple line is for the settled contact with $\delta_{T1}^* = 1.1\delta_{TS}^*$, and the brown dotted line represents the mean contact pressure for the onset of yield, i.e., $p_{mc}^* = 1.17$ when the Poisson's ratio $\nu = 0.42$.

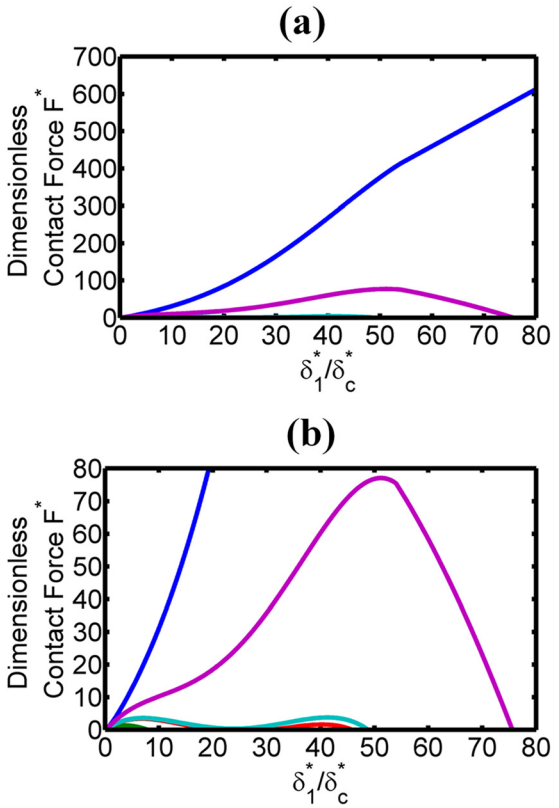

FIG. 6. (a) Dimensionless contact force F^* vs. δ_1^*/δ_c^*, (b) zoomed figure of (a): the blue line is for the first contact event; the green line is for the settled contact with $\delta_{T1}^* = 2\delta_{TS}^*$; the red line is for the settled contact with $\delta_{T1}^* = 1.47\delta_{TS}^*$; the light blue line is for the settled contact with $\delta_{T1}^* = 1.45\delta_{TS}^*$, and the purple line is for the settled contact with $\delta_{T1}^* = 1.1\delta_{TS}^*$.

residual depth is produced prior to the subsequent contact event if the elastoplastic or plastic deformation occurs in the first contact event. This residual depth can lead to a large difference in contact forces between the first and subsequent contact events in one switching cycle.

B. Comparison of modeling results and experimental data

Generally, the contact radius at the switch settled state is greater than the man-free-path length of electron in metals, i.e., $a \gg \lambda$. It results in the Sharvin resistance to be neglected, i.e., $\Omega_{SH} = 4\rho_e\lambda/3\pi a^2 \approx 0$,[22,23] where ρ_e is the electrical resistivity of the contact material. In addition, Berman *et al.*[24] demonstrated that absorbed organic contamination which forms adjacent to the direct contact region can suppress tunneling contributions, consequently increasing the contact resistance of a MEMS switch. Such contamination increases with switching cycles to cause the contamination-induced resistance to monotonically increase. However, this contamination-induced resistance is also neglected in the following analysis because the contact resistance evolution is dominated by the variation of contact radius according to our experimental observation. Thus in this study, only the Maxwell spreading resistance[25] is considered: $\Omega = \rho_e/2a_S$, where a_S is the contact radius at the switch settled state. Then the dimensionless contact resistance is defined as

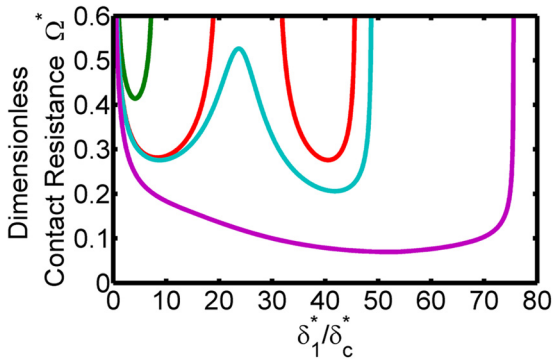

FIG. 7. Dimensionless contact resistance Ω^* vs. δ_1^*/δ_c^*: the green line is for the settled contact with $\delta_{T1}^* = 2\delta_{TS}^*$; the red line is for the settled contact with $\delta_{T1}^* = 1.47\delta_{TS}^*$; the light blue line is for the settled contact with $\delta_{T1}^* = 1.45\delta_{TS}^*$, and the purple line is for the settled contact with $\delta_{T1}^* = 1.1\delta_{TS}^*$.

$$\Omega^* = \frac{3\Omega\pi RY}{4E^*\rho_e} = \frac{1}{2a_S^*}. \tag{42}$$

Figure 7 illustrates the dimensionless contact resistance Ω^* versus δ_1^*/δ_c^* for the cases in Fig. 4. It is noted that the beginning value of dimensionless contact resistance shall be calculated according to such measured parameters although the initial values shown in Fig. 7 start at 0.6. It is also noted that the increase in δ_1^* is related to the increase in switching cycles. The modeling results show that the lifetime of a switch will be longer if δ_{T1}^* is designed to be close to δ_{TS}^* as the purple line.

Figure 8 shows the experimental results with different operating applied voltages. It is noted again that the number of switching cycles is related to δ_1^*. In Fig. 8(a), only Situation 1 is observed at three different recorded applied voltages. In Fig. 8(b), only Situation 2 occurs at three recorded applied voltages. In Fig. 8(c), two different situations were recorded: Situation 1 is observed for the recorded applied voltage of 29 V, and Situation 3 occurs for the recorded applied voltages of 34 and 39 V. By qualitatively comparing the experimental data to the modeling results, the experimental result (green line) of the recorded applied voltage of 29 V in Fig. 8(c) can be analogous to the green line ($\delta_{T1}^* = 2\delta_{TS}^*$) in Fig. 7. The experimental results (blue and red lines) of the recorded applied voltages of 34 and 39 V in Fig. 8(c) have the similar behavior as the red line ($\delta_{T1}^* = 1.47\delta_{TS}^*$) in Fig. 7.

The qualitative comparison of the modeling results in Fig. 7 and the experimental data in Fig. 8 indicates that the plastic deformation occurs around the contact region of a MEMS switch under hot switching in its lifetime. The contact damage becomes worse with switching cycles increasing. This phenomenon implies that the hot switching condition results in the local temperature around the contact region to rise and change the material properties, such as the elastic modulus and the yield strength. It is noted that the experimental results shown in Fig. 8 are measured from switches with permanent-open failure. For switches with permanent-closed failure as shown in Fig. 9, the contact resistance evolution was also observed with the same behavior including these three situations.

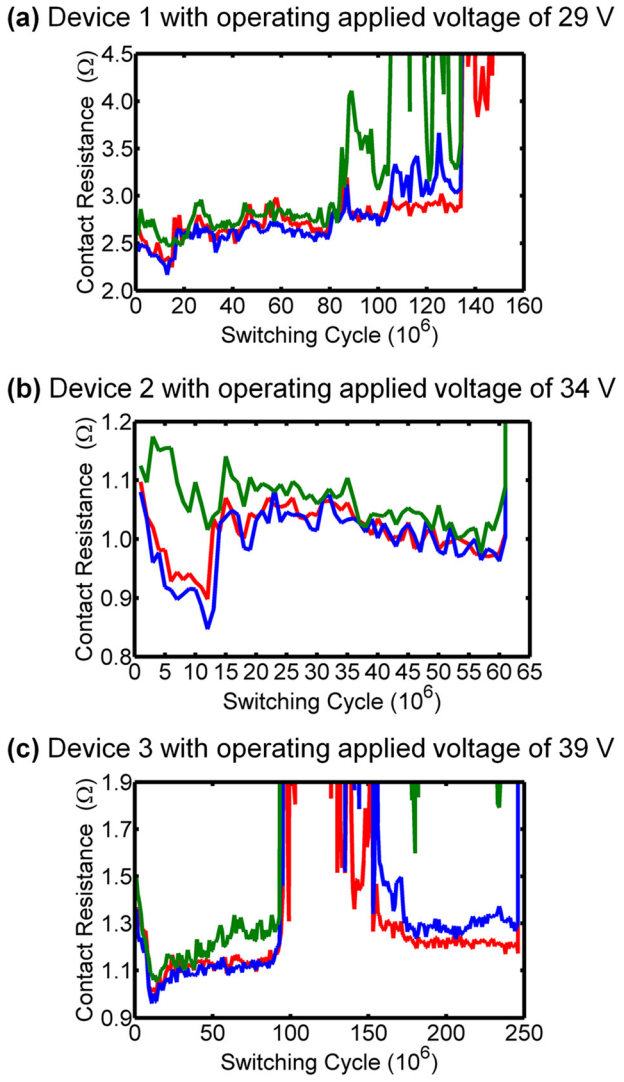

FIG. 8. Measured contact resistance vs. switching cycles for the switches with permanent-open failure: the green line is for the recorded applied voltage of 29 V; the blue line is for the recorded applied voltage of 34 V, and the red line is for the recorded applied voltage of 39 V.

V. CONCLUSION

A non-adhesive contact model has been developed to describe the contact behavior evolution in MEMS switches. During a single switching cycle, the switch tip can completely recover after unloading of the first contact event if the first contact event is elastic. Subsequent contact events are also elastic. If the elastoplastic or plastic deformation occurs in the first contact event, a residual depth will be produced between the switch tip and the drain prior to the subsequent contact event. This model shows that the contact behavior depends on the difference in the contact-free displacements between the first contact event and the settled contact events. The modeling results qualitatively agree with the experimental observations. Comparing the modeling results to the experimental data indicates that the hot switching condition causes the local temperature to rise and change the material properties around the contact region of a MEMS switch. This change results in contact damage to become worse with switching cycles increasing.

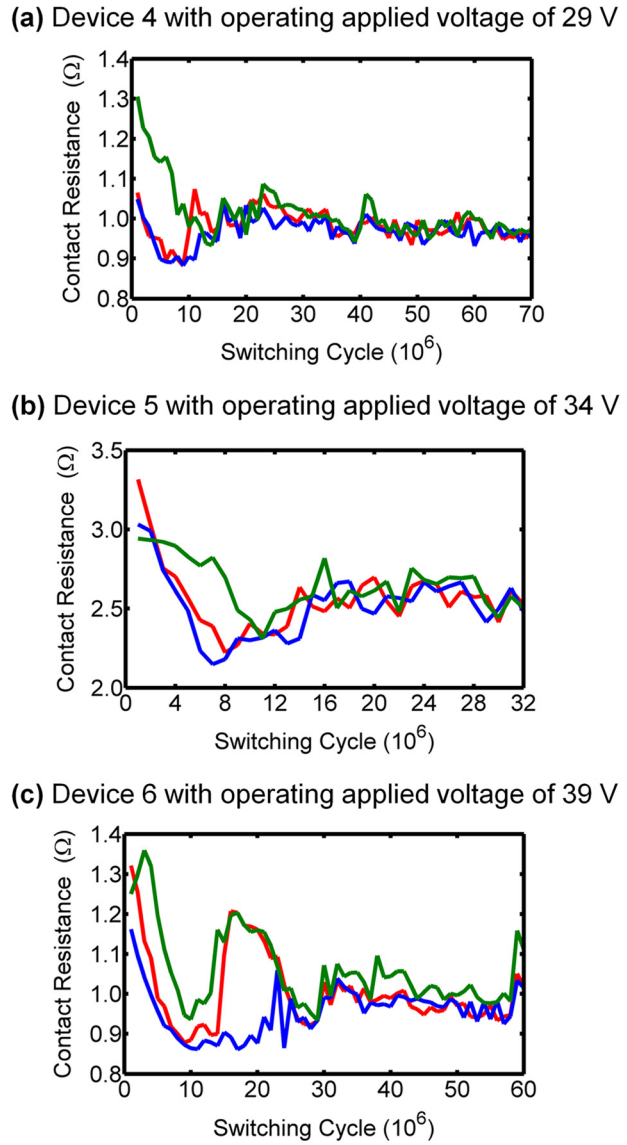

FIG. 9. Measured contact resistance vs. switching cycles for the switches with permanent-closed failure: the green line is for the recorded applied voltage of 29 V; the blue line is for the recorded applied voltage of 34 V, and the red line is for the recorded applied voltage of 39 V.

ACKNOWLEDGMENTS

This work has been supported by the NSF EARS: Spectrally Aware Interference Tolerant RF Nanosystems Program (ECCS-1247893) and the Center for Electronic Defense Systems (CEDS) at Purdue University.

[1]S. Majumder, N. McGruer, and G. G. Adams, in *2003 International Joint Tribology Conference, STLE/ASME* (2003), p. 79.
[2]S. Majumder, N. McGruer, and G. G. Adams, in *18th IEEE International Conference, MEMS 2005* (2005), p. 215.
[3]N. McGruer, G. Adams, L. Chen, Z. Guo, and Y. Du, in *19th IEEE International Conference, MEMS 2006* (2006), p. 230.
[4]R. Hennessy, A. Basu, G. Adams, and N. McGruer, J. Micromech. Microeng. **23**, 055003 (2013).
[5]B. D. Jensen, L. L.-W. Chow, K. Huang, K. Saitou, J. L. Volakis, and K. Kurabayashi, J. Microelectromech. Sys. **14**, 935 (2005).
[6]D. Berman, M. Walker, and J. Krim, J. Appl. Phys. **108**, 044307 (2010).
[7]A. Broue, J. Dhennin, P. Charvet, P. Pons, N. B. Jemaa, P. Heeb, F. Coccetti, and R. Plana, in *Proceedings of the 56th IEEE Holm Conference* (2010), p. 1.
[8]W. Chang, I. Etsion, and D. Bogy, J. Tribol. **109**, 257 (1987).
[9]Y. Zhao, D. M. Maietta, and L. Chang, J. Tribol. **122**, 86 (2000).
[10]L. Kogut and I. Etsion, J. Appl. Mech. **69**, 657 (2002).
[11]L. Kogut and I. Etsion, J. Colloid Interface Sci. **261**, 372 (2003).
[12]Y. Du, L. Chen, N. E. McGruer, G. G. Adams, and I. Etsion, J. Colloid Interface Sci. **312**, 522 (2007).
[13]Y. Du, G. G. Adams, N. E. McGruer, and I. Etsion, J. Appl. Phys. **103**, 064902 (2008).
[14]Z. Guo, N. McGruer, and G. Adams, J. Micromech. Microeng. **17**, 1899 (2007).
[15]A. Fruehling, W. Yang, and D. Peroulis, in *IEEE 25th International Conference on Micro Electro Mechanical System* (2012), p. 688.
[16]R. Tung, A. Fruehling, D. Peroulis, and A. Raman, J. Microelectromech. Sys. **23**, 137 (2014).
[17]O. Rezvanian, M. Zikry, C. Brown, and J. Krim, J. Micromech. Microeng. **17**, 2006 (2007).
[18]K. Johnson, *Contact Mechanics* (Cambridge University Press, 1985).
[19]J. Jamari and D. Schipper, Tribol. Lett. **21**, 262 (2006).
[20]A. Fruehling, W. Yang, and D. Peroulis, in *2013 IEEE MTT-S International Microwave Symposium Digest* (2013), p. 1.
[21]C. Poulain, A. Peschot, M. Vincent, and N. Bonifaci, in *2011 IEEE 57th Holm Conference on Electrical Contacts, Holm* (2011), p. 1.
[22]A. Jansen, A. Van Gelder, and P. Wyder, J. Phys. C: Solid State Phys. **13**, 6073 (1980).
[23]B. Nikolić and P. B. Allen, Phys. Rev. B **60**, 3963 (1999).
[24]D. Berman, M. Walker, C. Nordquist, and J. Krim, J. Appl. Phys. **110**, 114307 (2011).
[25]R. Holm and E. Holm, *Electric Contacts: Theory and Application* (Springer-Verlag, New York, 1967).